

# Highly Porous Thermoelectric Nanocomposites with Low Thermal Conductivity and High Figure of Merit from Large-Scale Solution-Synthesized $\text{Bi}_2\text{Te}_{2.5}\text{Se}_{0.5}$ Hollow Nanostructures

Biao Xu, Tianli Feng, Matthias T. Agne, Lin Zhou, Xiulin Ruan, G. Jeffery Snyder, and Yue Wu\*

**Abstract:** To enhance the performance of thermoelectric materials and enable access to their widespread applications, it is beneficial yet challenging to synthesize hollow nanostructures in large quantities, with high porosity, low thermal conductivity ( $\kappa$ ) and excellent figure of merit ( $zT$ ). Herein we report a scalable (ca. 11.0 g per batch) and low-temperature colloidal processing route for  $\text{Bi}_2\text{Te}_{2.5}\text{Se}_{0.5}$  hollow nanostructures. They are sintered into porous, bulk nanocomposites (phi 10 mm  $\times$  h 10 mm) with low  $\kappa$  ( $0.48 \text{ W m}^{-1} \text{ K}^{-1}$ ) and the highest  $zT$  (1.18) among state-of-the-art  $\text{Bi}_2\text{Te}_{3-x}\text{Se}_x$  materials. Additional benefits of the unprecedented low relative density (68–77%) are the large demand reduction of raw materials and the improved portability. This method can be adopted to fabricate other porous phase-transition and thermoelectric chalcogenide materials and will pave the way for the implementation of hollow nanostructures in other fields.

Hollow nanostructures have attracted continuously interest in diverse fields, such as batteries,<sup>[1]</sup> supercapacitors,<sup>[2]</sup> biomedicine,<sup>[3]</sup> catalysis,<sup>[4]</sup> photocatalysis,<sup>[5]</sup> sensors,<sup>[6]</sup> and optics,<sup>[7]</sup> because their hollow interiors can act as containers and provide a large number of reactive sites due to their high specific surface area.<sup>[8]</sup> To synthesize hollow nanostructures, hard-templating (e.g. against silica nanoparticles<sup>[9]</sup>) or polystyrene nanobeads<sup>[10]</sup>) and self-templating (e.g. Kirkendall effect<sup>[11]</sup>) are widely investigated. The self-templating synthesis is more straightforward and easier to scale up. The large-scale production, in conjunction with exploring how to use the hollow nanostructures, can lead to their practical implementation.

Solid-state semiconductors can convert waste heat into electric power through the thermoelectric effect. Thermoelectric devices exhibit excellent reliability and portability,

representing a promising method of energy recovery.<sup>[12]</sup> The performance of a thermoelectric material is determined by its figure of merit,  $zT = S^2\sigma T/\kappa$ , where  $S$  is the Seebeck coefficient,  $\sigma$  is the electrical conductivity, and  $\kappa$  is the thermal conductivity. Recently, nanostructures have been extensively used to lower the  $\kappa$  and improve the  $zT$  of the thermoelectric materials.<sup>[13]</sup> It can be ascribed to the increased scattering of phonons with increasing grain boundary density. However, due to the commonly used high-temperature processes required to fabricate thermoelectric modules, grain growth is unavoidable, diminishing the structural effect on  $\kappa$ . Alternatively, porosity that arises from the irregular shape and imperfect stacking of building blocks at the nanoscale can offer an additional means to reduce the thermal conductivity, yet limitedly.<sup>[14]</sup> To further increase the porosity of a thermoelectric material, it might be an effective way to use hollow nanostructure as a powder precursor, as it intrinsically holds a large amount of void spaces. However, hollow nanostructures have been seldom used as thermoelectric materials due to the concern of significantly sacrificed electrical conductivity.<sup>[15]</sup> There has not been any complete evaluation of the figure of merit on the bulk scale ( $> 10 \text{ g}$ ).

Herein, we report the first example of the scalable (ca. 11 g per batch), self-templating synthesis of  $\text{Bi}_2\text{Te}_{2.5}\text{Se}_{0.5}$  hollow nanostructures and the subsequent sintering of them into highly porous thermoelectric nanocomposites. The as-sintered material is 32% porous and holds an ultralow thermal conductivity. Consequently, its  $zT$  is comparable to the best  $\text{Bi}_2\text{Te}_{3-x}\text{Se}_x$ . This approach can reduce the demand in raw material and provide better portability due to the light weight compared to conventional fully dense thermoelectric materials.

The multistep synthesis is inspired by our previous method to synthesize  $\text{Bi}_2\text{Te}_3$  nanowires.<sup>[16]</sup> In step 1, tellurium dioxide ( $\text{TeO}_2$ ), selenium dioxide ( $\text{SeO}_2$ ), potassium hydroxide (KOH), and polyvinylpyrrolidone (PVP) were dissolved into ethylene glycol (EG). Then hydrazine hydrate ( $\text{N}_2\text{H}_4 \cdot \text{H}_2\text{O}$ ) was injected and the solution turned dark blue. This mixture was heated at  $110^\circ\text{C}$  for 1 h, for the formation of Te-Se nanorods (Figure 1a). In step 2, anhydrous hydrazine ( $\text{N}_2\text{H}_4$ ) and a stock solution of  $\text{Bi}(\text{NO}_3)_3 \cdot 5\text{H}_2\text{O}$  were injected into this dispersion sequentially to form the Bi-Te-Se nanorods (Figure 1b). This dispersion was heated at  $110^\circ\text{C}$  for another hour. In step 3, the temperature was raised to  $140^\circ\text{C}$  and maintained for 3 h to yield BiTeSe hollow nanorods (Figure 1c).

To characterize the intermediate products, several investigations were conducted. First, X-ray diffraction (XRD) was used to study the crystal phases. After step 1, the product

[\*] Dr. B. Xu, Prof. Dr. Y. Wu  
Department of Chemical and Biological Engineering  
Iowa State University, Ames, IA 50011 (USA)  
E-mail: yuewu@iastate.edu

T. L. Feng, Prof. Dr. X. L. Ruan  
Department of Mechanical Engineering, Purdue University  
West Lafayette, IN 47907 (USA)

M. T. Agne, Prof. Dr. G. J. Snyder  
Department of Materials Science and Engineering  
Northwestern University, Evanston, IL 60208 (USA)

Dr. B. Xu, Prof. Dr. L. Zhou, Prof. Dr. Y. Wu  
Ames Laboratory, Department of Energy  
Ames  
IA 50011 (USA)

Supporting information for this article can be found under:  
<http://dx.doi.org/10.1002/anie.201612041>.

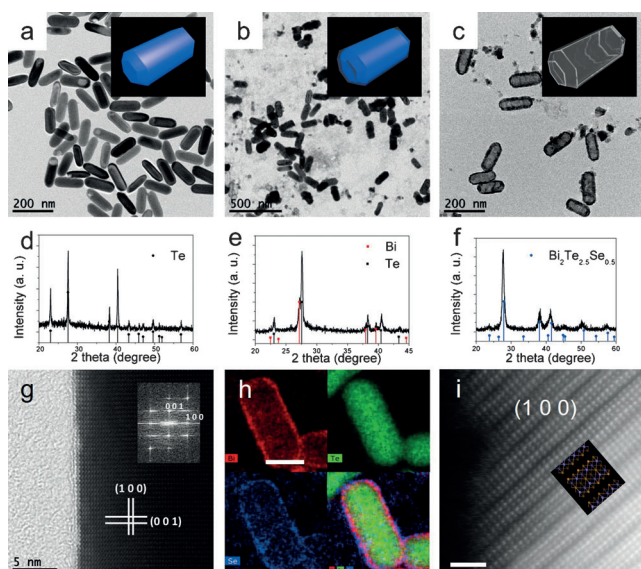


**Figure 1.** Low-magnification TEM images of a) Te nanorods (step 1), b) Te@Bi-Se core-shell nanorods (step 2), and c)  $\text{Bi}_2\text{Te}_{2.5}\text{Se}_{0.5}$  hollow nanorods (step 3), d–f) XRD profiles of the products in each step, g) HRTEM image of the Te nanorods, h) EDS elemental mapping of the Te@Bi-Se core-shell nanorods, scale bar 50 nm, i)  $C_s$ -corrected HAADF-STEM image of the  $\text{Bi}_2\text{Te}_{2.5}\text{Se}_{0.5}$  hollow nanostructures and the corresponding atomic model of (100) surface, Bi, purple, Te(Se), orange, scale bar 1 nm.

could be indexed to pure trigonal tellurium (JCPDS number 36-1452, Figure 1 d). After step 2, hexagonal bismuth (JCPDS number 44-1246) was found because anhydrous hydrazine-reduced  $\text{Bi}^{\text{III}}(\text{NO}_3)_3$  to  $\text{Bi}^0$ . Meanwhile,  $\text{Te}^0$  was still retained (Figure 1 e). Finally, in step 3, Bi and Te (Se) reacted with each other to form hexagonal  $\text{Bi}_2\text{Te}_{2.5}\text{Se}_{0.5}$  (JCPDS number 51-0643, Figure 1 f). Transmission electron microscopy (TEM) provided more details about the microstructures of these intermediate products. After step 1, Te nanorods were formed (Figure 1 a). Statistics on multiple nanorods revealed that the length was  $150 \pm 10$  nm and the diameter was  $50 \pm 4$  nm. The (001) plane was found to be perpendicular to the axial direction of the nanorod (Figure 1 g). After step 2, the surface of the nanorods became very rough (Figure 1 b). The length was elongated to  $170 \pm 15$  nm and the diameter was enlarged to  $60 \pm 8$  nm. Combining the increased size of the nanorods with the result of XRD ( $\text{Bi}^0 + \text{Te}^0$ , Figure 1 e), we speculated that  $\text{Bi}^0$  had deposited onto the surface of the Te nanorod. Energy dispersive spectroscopy (EDS) elemental mapping apparently proved that the core was composed of Te while the shell was comprised of Bi and Se (Figure 1 h). After step 3, all the nanorods were found to transform to hollow shells. The outer diameter was  $60 \pm 8$  nm, the length was  $180 \pm 15$  nm and the average thickness of the shell was  $12 \pm 3$  nm (Figure 1 c). EDS elemental mapping indicated that Bi, Te, and Se were uniformly distributed in the hollow nanostructure (see Figure S1f in the Supporting Information). At the tip ends, the (006) plane of  $\text{Bi}_2\text{Te}_{2.5}\text{Se}_{0.5}$  was observed perpendicular to the axial direction (Figure S1e). The atomic structure can be clearly depicted in the  $C_s$ -corrected HAADF

STEM image, when referred to a proposed atomic structure of  $\text{Bi}_2\text{Te}_{2.5}\text{Se}_{0.5}$  (100) in Figure 1 i.

Scanning electron microscopy (SEM) further verified the morphologies of the products step by step (Figure S2). Additionally, EDS revealed the compositions of these products. After step 1, the atomic ratio of Te:Se was 96.0:4.0. According to the precursor ratio of Te:Se (83.33:16.67), Se was only partially (ca. 1/5) converted. After step 2, Bi:Te:Se = 37.64:51.64:10.69.  $[\text{Te} + \text{Se}]/\text{Bi} = 1.66$ , while the nominal ratio was 1.50, indicating that Bi was deficient in the product. In this Te@Bi-Se core-shell structure, Te:Se = 4.83:1, which was quite close to the nominal ratio of 5:1. After step 3, Bi:Te:Se = 41.22:50.23:9.54.  $[\text{Te} + \text{Se}]/\text{Bi} = 1.45$ , which was nearly the same as the nominal 1.50 ratio. In this final  $\text{Bi}_2\text{Te}_{2.5}\text{Se}_{0.5}$  hollow nanostructure, Te:Se = 5.27:1 and this was also approximate to 5:1 of the precursors.

Based on the aforementioned characterizations, we attempted to clarify the formation mechanisms of the  $\text{Bi}_2\text{Te}_{2.5}\text{Se}_{0.5}$  hollow nanorod. As stated before, after the 2nd step, the Te@Bi-Se (core@shell) structure was formed. We found that a small portion of them transformed to a partially hollow structure (Figure S1b and d). In this intermediate structure, the Te-Se core nanorod reacted and became concaved in the equatorial region. The corresponding region of the shell showed a layered structure of  $\text{Bi}_2(\text{Te}_x\text{Se}_{1-x})_3$  (Figure S1d), indicating that the reaction between Bi and Te (Se) had started. To form the  $\text{Bi}_2(\text{Te}_x\text{Se}_{1-x})_3$  shell, Te atoms had to diffuse outward and Bi(Se) atoms inward across the interface, reacting with each other. The Kirkendall effect might play a role in this process. Generally, the diffusion flow is expressed as follows Equation (1),<sup>[17]</sup>

$$|J_i| = \frac{D_i \Delta C_i}{r^2} \frac{r_{\text{in}}(t) r_{\text{out}}(t)}{r_{\text{out}}(t) - r_{\text{in}}(t)} \quad (1)$$

where  $J_i$  is the magnitude of the flux,  $D_i$  is the diffusion coefficient,  $\Delta C_i$  is the difference of concentration across the interface, for species  $i$ ,  $r_{\text{in}}$  and  $r_{\text{out}}$  are the diameters of the inner (Te/ $\text{Bi}_2\text{Te}_3$ ) and outer interface ( $\text{Bi}_2\text{Te}_3/\text{Bi}$ ), respectively. As the atomic radius of Te (140 pm) is much smaller than that of Bi (160 pm),  $D_{\text{Te}}$  could be larger than  $D_{\text{Bi}}$ . Moreover, to form stoichiometric  $\text{Bi}_2\text{Te}_3$ , three atoms of Te had to diffuse out and only two of Bi in. As the initial  $\Delta C_{\text{Te}}:\Delta C_{\text{Bi}}$  was 3:2 (determined by precursors), this ratio would be maintained as 3:2. Therefore,  $J_{\text{Te,out}}$  should be larger than  $J_{\text{Bi,in}}$  throughout the process and the inner core of Te would become void during the diffusion–reaction process (Figure S1c). Finally, during the 3rd step, as the temperature was increased to 140 °C, the diffusion and reaction were completed. Resultantly, all the nanorods became hollow.

The scalable (11.0 g, Figure 2 a) synthesis of  $\text{Bi}_2\text{Te}_{2.5}\text{Se}_{0.5}$  hollow nanostructures enabled us to fabricate bulk nanocomposites and study their thermoelectric properties. The as-obtained dispersion of hollow nanorods was centrifuged, dried under vacuum, and pulverized. This powder was spark plasma sintered (SPSed) into a phi-10 mm cylinder and a pellet (Figure 2 b). For the 400 °C-sintered sample, the mass density was  $5.30 \text{ g cm}^{-3}$  and the relative density was 67.9%, among the lowest reported for  $\text{Bi}_2\text{Te}_{3-x}\text{Se}_x$ -based

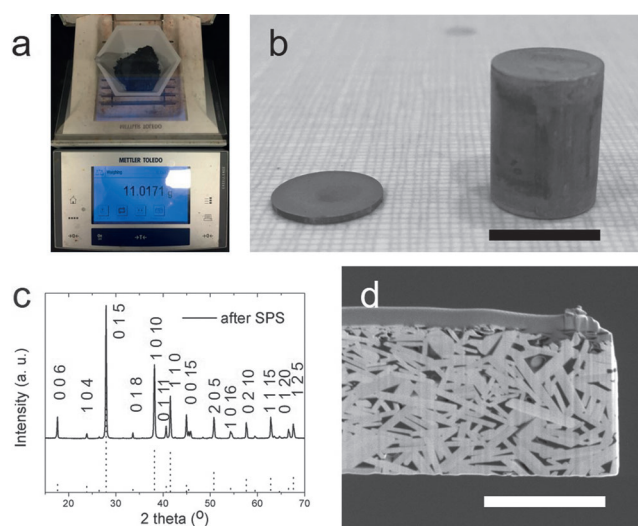


**Figure 2.** a) 11.0 g of the hollow nanostructure product, b) 400°C-sintered pellet and cylinder, scale bar 10 mm, c) XRD profile of the 400°C-sintered pellet, d) SEM of the FIB-cut specimen from the 400°C-sintered disk, scale bar 2 μm.

thermoelectric materials (Table 1). For the 350°C-sintered sample, the mass density was 6.02 g cm<sup>-3</sup> and the relative density was 77.2%. The as-sintered nanocomposite was then comprehensively characterized. The XRD profile showed typical reflection peaks of Bi<sub>2</sub>Te<sub>2.5</sub>Se<sub>0.5</sub> (JCPDS number 51-0643, Figure 2c). EDS confirmed a composition of Bi<sub>2.02</sub>Te<sub>2.56</sub>Se<sub>0.44</sub>. From the SEM image of a focused-ion-beam (FIB) cut sample (Figure 2d), we found that the starting

nanoshells were crushed and re-pressed into a highly porous material with larger grains.

The thermoelectric properties of the SPSed Bi<sub>2.02</sub>Te<sub>2.56</sub>Se<sub>0.44</sub> nanocomposites were then measured along the out-of-plane direction and the results were shown in Figure 3. The electrical conductivities ( $\sigma$ ) of the 350°C- and 400°C-sintered samples were displayed in Figure 3a. For the 400°C-sintered sample,  $\sigma$  decreased from  $8.13 \times 10^4$  S m<sup>-1</sup> at 313 K, monotonically with increasing temperature, to  $4.93 \times 10^4$  S m<sup>-1</sup> at 513 K. This indicated the behavior of a degenerate semiconductor. The carrier concentration was extracted through Hall effect measurement ( $n_{\text{H}} \approx 7.0 \times 10^{19}$  cm<sup>-3</sup>, Figure S3a). Hall coefficient was negative and nearly constant, confirming that our nanocomposite was heavily doped to n-type. Electron mobility  $\mu$  was calculated as  $\mu = \sigma/n_{\text{H}}e$  and exhibited in Figure S3b.

The Seebeck coefficient ( $S$ ) had a negative sign, agreeing well with the Hall effect measurement. The absolute value of  $S$  increased monotonically with respect to temperature (Figure 3a). However, the slope became smaller and a plateau in  $S$  was achieved in the high-temperature range. This is typical of bipolar conduction, where thermal excitation of the minority carriers (hole) contributes negatively to the total  $S$ . The power factor was calculated as  $S^2\sigma$  (Figure 3b). Throughout the temperature of interest,  $S^2\sigma$  of the 400°C-sintered sample showed a very small change and the peak value was 1.28 mW m<sup>-1</sup> K<sup>-2</sup> at 438 K. The total thermal conductivity was calculated through  $\kappa_{\text{tot}} = D_{\text{T}}C_p\rho$ , where  $D_{\text{T}}$  (thermal diffusivity) could be measured from the laser flash method (Figure S3c),  $C_p$  (specific heat) was obtained by a differential scanning calorimeter (DSC, Figure S3d) and  $\rho$  (density) was determined from the mass and geometry. The temperature dependence of  $\kappa_{\text{tot}}$  is displayed in Figure 3b. For the 400°C-sintered sample,  $\kappa_{\text{tot}}$  decreased from 0.66 W m<sup>-1</sup> K<sup>-1</sup> at 313 K to 0.59 W m<sup>-1</sup> K<sup>-1</sup> at 438 K, and then increased again to 0.62 W m<sup>-1</sup> K<sup>-1</sup> at 538 K. For the 350°C-sintered sample,  $\kappa_{\text{tot}}$  achieved its minimum value of 0.48 W m<sup>-1</sup> K<sup>-1</sup> at 438 K.

Finally,  $zT$  is calculated as  $S^2\sigma T \kappa^{-1}$  and its temperature dependence is plotted in Figure 3d. For the 350°C-sintered sample, the  $zT$  at 313 K is 0.61 and increases steadily with temperature, reaching the peak of 1.18 at 463 K. The  $zT$  of  $> 1.0$  is maintained from 388 K to 513 K. For the 400°C-sintered sample, the highest  $zT$  also reaches 1.0.

We then conduct theoretical modeling to clarify the origin of the decent figure of merit of our porous BiTeSe nanocomposite. It is mainly ascribed to the high porosity and low thermal conductivity.

**Table 1:** Properties of our Bi<sub>2</sub>Te<sub>3-x</sub>Se<sub>x</sub> materials as compared with literature values.

	Sintering condition	Relative density	$\kappa_{\text{lat,min}}$ [W m <sup>-1</sup> K <sup>-1</sup> ]	Carrier mobility [cm <sup>2</sup> V <sup>-1</sup> s <sup>-1</sup> ]	$\mu_{\text{H}}/\kappa_{\text{L}} \cdot (m^*/m_0)^{3/2}$ [ $10^{-3}$ m <sup>3</sup> K V <sup>-1</sup> s <sup>-1</sup> W <sup>-1</sup> ]	$zT_{\text{max}}$
This work	400°C, 40 MPa, 5 min	<b>67.9%</b>	<b>0.13</b>	71 (313 K)	19.5 (313 K)	1.00 (488 K)
	350°C, 40 MPa, 5 min	<b>77.2%</b>	<b>0.14</b>	68 (313 K)	17.3 (313 K)	<b>1.18</b> (463 K)
Ren, 2010 <sup>[18]</sup>	500°C, 2 min	87%	N/A	N/A	N/A	1.04 (398 K)
Xiong, 2012 <sup>[19]</sup>	250°C, 40 MPa, 5 min	87%	0.45	N/A	N/A	0.55 (300 K)
Zhao, 2015 <sup>[20]</sup>	400°C, 80 MPa, 30 min	97%	0.52	157 (300 K)	56 (300 K)	1.20 (360 K)
Li, 2016 <sup>[21]</sup>	460°C, 50 MPa, 5 min	97%	0.40	152 (300 K)	30 (300 K)	1.10 (470 K)
Zou, 2016 <sup>[22]</sup>	250°C, 40 MPa, 5 min	92.6%	0.36	250 (300 K)	N/A	1.23 (470 K)

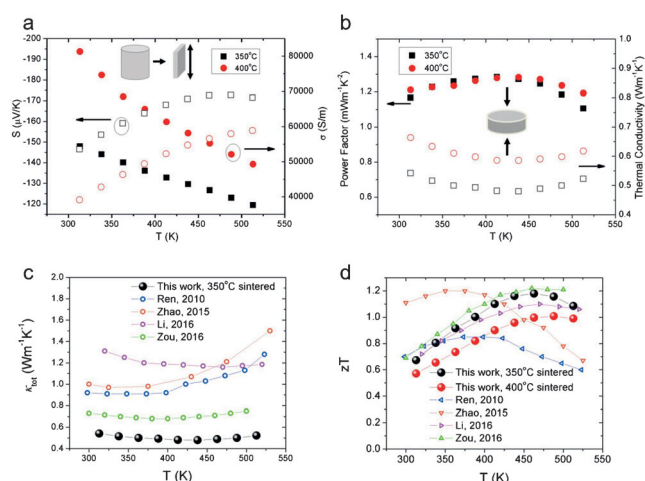


**Figure 3.** Temperature dependence of a) Seebeck coefficients ( $S$ , hollow markers) and electrical conductivities ( $\sigma$ , solid markers), b) power factors ( $S^2\sigma$ , solid markers) and thermal conductivities ( $\kappa_{\text{tot}}$ , hollow markers). c)  $\kappa_{\text{tot}}$  and d)  $zT$  of the porous nanocomposite in this work compared with previously reported  $\text{Bi}_2\text{Te}_{3-x}\text{Se}_x$ .<sup>[18–22]</sup> Also see Table 1 for more details.

Based on the effective medium theory,<sup>[23]</sup> the lattice thermal conductivity of a porous material is expressed in Equation (2),

$$\kappa_l = (1 - P)^{3/2} \kappa_{lf} \quad (2)$$

where  $\kappa_{lf}$  is the lattice thermal conductivity of the imaginary fully dense material,  $P$  is the porosity ( $P = 1 - \rho/\rho_0$ ,  $\rho/\rho_0$  is the relative density). For our 400°C-sintered sample,  $\kappa_l = \kappa_{lf}/1.78$  (Figure 4b). The lattice thermal conductivity of the imaginary fully dense nanocomposite  $\kappa_{lf}$  is then calculated by the phonon Boltzmann transport Equation (3).<sup>[24]</sup>

$$\kappa_{lf} = \frac{4\pi}{3} \frac{1}{(2\pi)^3} \sum_j \left[ \frac{2}{3} \int_x + \frac{1}{3} \int_z \right] \frac{\hbar^2 \omega^2(\mathbf{k}, j)}{k_B T^2} \frac{e^{-\frac{\hbar\omega(\mathbf{k}, j)}{k_B T}}}{\left( e^{\frac{\hbar\omega(\mathbf{k}, j)}{k_B T}} - 1 \right)^2} \quad (3)$$

$$\cdot v^2(\mathbf{k}, j) \tau_{\text{ph}}(\mathbf{k}, j) k^2 dk$$

To obtain  $\kappa_{lf}$  with Equation (3), we need to know the phonon frequency  $\omega$ , the phonon group velocity  $v$ , and the phonon relaxation time  $\tau_{\text{ph}}$  at the wave-vector  $\mathbf{k}$  and branch  $j$ .  $\omega$  and  $v$  are obtained from first principles calculations using density functional theory (DFT),<sup>[25]</sup> and  $\tau_{\text{ph}}$  is calculated from the Matthiessen rule in Equation (4).

$$\tau_{\text{ph}}^{-1}(\mathbf{k}, j) = \tau_{\text{anh}}^{-1}(\mathbf{k}, j) + \tau_{\text{mass}}^{-1}(\mathbf{k}, j) + \tau_{\text{coupl}}^{-1}(\mathbf{k}, j) + \tau_{\text{DC}}^{-1}(\mathbf{k}, j) + \tau_{\text{DS}}^{-1}(\mathbf{k}, j) + \tau_{\text{B}}^{-1}(\mathbf{k}, j) \quad (4)$$

The terms on the right hand side are the scattering rates induced by the lattice anharmonicity (anh), Te-Se alloy mass disorder (mass), coupling between anharmonic phonon scattering and mass disorder scattering (coupl), dislocation core (DC), dislocation strain (DS), and grain boundaries (B), respectively. The detailed calculations of them can be found in

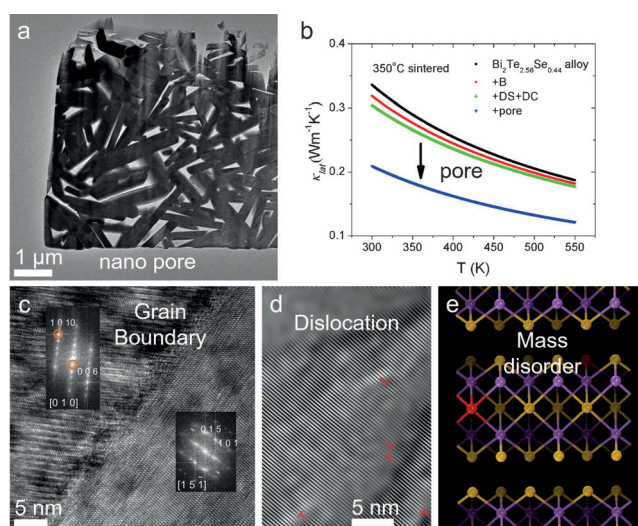


**Figure 4.** a) TEM image of the porous  $\text{Bi}_{2.02}\text{Te}_{2.56}\text{Se}_{0.44}$  nanocomposite (400°C-sintered), b) theoretical modeling of  $\kappa_{\text{lattice}}$  of the 350°C-sintered  $\text{BiTeSe}$  nanocomposite, c) HRTEM image showing a grain boundary, d) inverse fast Fourier transform (IFFT) of a HRTEM image showing dislocations, e) scheme on alloy mass disorder; bismuth (purple), tellurium (orange), and selenium (red).

the Supporting Information. The parameters involved were determined from various experiments (Table S1). The lattice anharmonicity was extracted from a previous study on bulk-grain  $\text{Bi}_2\text{Te}_3$  and  $\text{Bi}_2\text{Se}_3$ .<sup>[26]</sup> The extent of Te-Se mass disorder was determined from EDS. Dislocations were observed from TEM (Figure 4d). The dislocation densities were  $5.0 \times 10^{11} \text{ cm}^{-2}$  and  $7.6 \times 10^{11} \text{ cm}^{-2}$ , for the 350°C- and 400°C-sintered sample, respectively. Grain boundary was also studied by TEM (Figure 4c). Low-magnification TEM (Figure 4a) and SEM images (Figure S2d) revealed that the grains were big flakes with diameter around 1.5  $\mu\text{m}$  for the 400°C-sintered sample (1.2  $\mu\text{m}$  for the 350°C-sintered one) and thickness around 300 nm for the 400°C-sintered sample (250 nm for the 350°C-sintered one).

Based on the modeling, we have found that the ultralow lattice thermal conductivity is benefited from the broad-range phonon frequency scattering and the large porosity. At 463 K where  $zT$  reached its maxima for the 350°C-sintered sample, the lattice thermal conductivity of bulk-grain  $\text{Bi}_2\text{Te}_{2.56}\text{Se}_{0.44}$  ( $0.71 \text{ W m}^{-1} \text{ K}^{-1}$ ) was reduced by the grain boundary, dislocation, mass-disorder and coupling scatterings to  $0.21 \text{ W m}^{-1} \text{ K}^{-1}$ , which was then further diminished by the pores (Figure 4a) to  $0.14 \text{ W m}^{-1} \text{ K}^{-1}$  (Figure 4b). Due to the extremely low relative density and high porosity (Table 1), the  $\kappa_{\text{lat}}$  of our material was very low (Table 1; lat = lattice). Consequently, the  $\kappa_{\text{total}}$  of our highly porous  $\text{BiTeSe}$  is also the lowest among those in literatures<sup>[18–22]</sup> (Figure 3c), from RT to 513 K. Although the dislocation, grain boundary, and pores had reduced the lattice thermal conductivity to a large extent, the electron mobility of our porous  $\text{BiTeSe}$  material was still maintained quite high (Table 1), possibly due to the large grain size and high crystallinity. Thus, the quality factor,  $\mu_{\text{H}}/\kappa_{\text{L}}(m^*/m^0)^{3/2}$ , was as high as those of previously reported  $\text{BiTeSe}$ <sup>[21]</sup> (Table 1) and the  $zT$  of our highly porous  $\text{BiTeSe}$

nanocomposite (350°C-sintered) was higher than 1.0 from 388 to 513 K, making it suitable for converting waste heat to electricity.

Compared with state-of-the-art n-type BiTeSe materials, our highly porous BiTeSe nanocomposite has comparable or even higher  $zT$  but uses nearly 1/3 less quantity of expensive raw materials (namely tellurium), reducing the overall production costs. Additionally, the extremely low mass density (67.9% or 77.2%) further enhances the portability of the thermoelectric module. These two advantages make our material suitable in practical use (e.g. powering wearable electronics) and niche application (e.g. power source in deep-space emission), respectively. Lastly, we emphasize that the low-temperature solution processing method is energy-saving when compared to the high- $T$  solid-state route commonly used in making other n-type materials, such as MgSiSn<sup>[27]</sup> and NaGaSn,<sup>[28]</sup> that are used in the same temperature range (300–500 K).

In conclusion, we have synthesized Bi<sub>2</sub>Te<sub>2.5</sub>Se<sub>0.5</sub> hollow nanostructures using a scalable (11.0 g) solution-phase route. The as-obtained nanopowder can be spark-plasma-sintered into a highly porous nanocomposite that exhibits a  $zT > 1$  in a wide temperature range (388–513 K). Through theoretical modeling, we find that the distinctly high porosity, as well as grain boundary, dislocation, and alloy mass disorder, lead to the extremely low thermal conductivity and high figure of merit. The ultralow relative density will also reduce the use of raw materials and improve the portability of the thermoelectric device. We expect that this approach can be readily adopted to fabricate other types of porous phase-transition and thermoelectric chalcogenide nanocomposites, such as Ag<sub>2</sub>Te, Cu<sub>2</sub>Te, PbTe, PbSe, and SnSe, and facilitate the use of hollow nanostructures in a variety of fields.

### Acknowledgements

B.X. and Y.W. gratefully thank for support from the Office of Naval Research, award number N00014-16-1-2066. T.L.F. and X.L.R. acknowledge the Defense Advanced Research Projects Agency (DARPA), award number HR0011-15-2-0037. M.T.A. and J.G.S. would like to acknowledge funding from the Solid-State Solar-Thermal Energy Conversion Centre (S3TEC), an Energy Frontier Research Centre funded by the U.S. Department of Energy, Office of Science, Basic Energy Sciences under award number DE-SC0001299. The TEM work (L.Z.) was performed at the Ames Laboratory under contract number DE-AC02-07CH11358 which is supported by the Materials Sciences Division of the Office of Basic Energy Sciences of the U.S. Department of Energy.

### Conflict of interest

The authors declare no conflict of interest.

**Keywords:** hollow nanostructures · Kirkendall effect · porous nanocomposites · thermal conductivity · thermoelectric materials

- [1] X. W. Lou, Y. Wang, C. Yuan, J. Y. Lee, L. A. Archer, *Adv. Mater.* **2006**, *18*, 2325–2329.
- [2] F. Xu, Z. Tang, S. Huang, L. Chen, Y. Liang, W. Mai, H. Zhong, R. Fu, D. Wu, *Nat. Commun.* **2015**, *6*, 7221.
- [3] X. Cai, W. Gao, M. Ma, M. Wu, L. Zhang, Y. Zheng, H. Chen, J. Shi, *Adv. Mater.* **2015**, *27*, 6382–6389.
- [4] S.-W. Kim, M. Kim, W. Y. Lee, T. Hyeon, *J. Am. Chem. Soc.* **2002**, *124*, 7642–7643.
- [5] J. Sun, J. Zhang, M. Zhang, M. Antonietti, X. Fu, X. Wang, *Nat. Commun.* **2012**, *3*, 1139.
- [6] H. Zhang, Q. Zhu, Y. Zhang, Y. Wang, L. Zhao, B. Yu, *Adv. Funct. Mater.* **2007**, *17*, 2766–2771.
- [7] S. E. Skrabalak, L. Au, X. Li, Y. Xia, *Nat. Protoc.* **2007**, *2*, 2182–2190.
- [8] X. Wang, J. Feng, Y. Bai, Q. Zhang, Y. Yin, *Chem. Rev.* **2016**, *116*, 10983–11060.
- [9] J. B. Joo, Q. Zhang, M. Dahl, I. Lee, J. Goebel, F. Zaera, Y. Yin, *Energy Environ. Sci.* **2012**, *5*, 6321–6327.
- [10] Z. Zhong, Y. Yin, B. Gates, Y. Xia, *Adv. Mater.* **2000**, *12*, 206–209.
- [11] a) Y. Yin, R. M. Rioux, C. K. Erdonmez, S. Hughes, G. A. Somorjai, A. P. Alivisatos, *Science* **2004**, *304*, 711–714; b) H. Fan, M. Knez, R. Scholz, K. Nielsch, E. Pippel, D. Hesse, M. Zacharias, U. Gosele, *Nat. Mater.* **2006**, *5*, 627–631.
- [12] a) W. G. Zeier, A. Zevalkink, Z. M. Gibbs, G. Hautier, M. G. Kanatzidis, G. J. Snyder, *Angew. Chem. Int. Ed.* **2016**, *55*, 6826–6841; *Angew. Chem.* **2016**, *128*, 6938–6954; b) J. R. Sootsman, D. Y. Chung, M. G. Kanatzidis, *Angew. Chem. Int. Ed.* **2009**, *48*, 8616–8639; *Angew. Chem.* **2009**, *121*, 8768–8792.
- [13] a) B. Poudel, Q. Hao, Y. Ma, Y. Lan, A. Minnich, B. Yu, X. Yan, D. Wang, A. Muto, D. Vashaee, X. Chen, J. Liu, M. S. Dresselhaus, G. Chen, Z. Ren, *Science* **2008**, *320*, 634–638; b) K. F. Hsu, S. Loo, F. Guo, W. Chen, J. S. Dyck, C. Uher, T. Hogan, E. K. Polychroniadis, M. G. Kanatzidis, *Science* **2004**, *303*, 818–821; c) M. S. Dresselhaus, G. Chen, M. Y. Tang, R. G. Yang, H. Lee, D. Z. Wang, Z. F. Ren, J. P. Fleurial, P. Gogna, *Adv. Mater.* **2007**, *19*, 1043–1053; d) R. Tangirala, J. L. Baker, A. P. Alivisatos, D. J. Milliron, *Angew. Chem. Int. Ed.* **2010**, *49*, 2878–2882; *Angew. Chem.* **2010**, *122*, 2940–2944; e) D. Ding, D. Wang, M. Zhao, J. Lv, H. Jiang, C. Lu, Z. Tang, *Adv. Mater.* **2016**, DOI: 10.1002/adma.201603444.
- [14] a) H. Lee, D. Vashaee, D. Z. Wang, M. S. Dresselhaus, Z. F. Ren, G. Chen, *J. Appl. Phys.* **2010**, *107*, 094308; b) Y. Zhang, T. Day, M. L. Snedaker, H. Wang, S. Krämer, C. S. Birkel, X. Ji, D. Liu, G. J. Snyder, G. D. Stucky, *Adv. Mater.* **2012**, *24*, 5065–5070.
- [15] R. Jin, G. Chen, J. Pei, *J. Phys. Chem. C* **2012**, *116*, 16207–16216.
- [16] S. W. Finet, H. Fang, H. Yang, H. Darsono, Y. Wu, *Nanoscale* **2014**, *6*, 7872–7876.
- [17] Y. Yin, C. K. Erdonmez, A. Cabot, S. Hughes, A. P. Alivisatos, *Adv. Funct. Mater.* **2006**, *16*, 1389–1399.
- [18] X. Yan, B. Poudel, Y. Ma, W. S. Liu, G. Joshi, H. Wang, Y. Lan, D. Wang, G. Chen, Z. F. Ren, *Nano Lett.* **2010**, *10*, 3373–3378.
- [19] A. Soni, Z. Yanyuan, Y. Ligen, M. K. K. Aik, M. S. Dresselhaus, Q. Xiong, *Nano Lett.* **2012**, *12*, 1203–1209.
- [20] L. Hu, H. Wu, T. Zhu, C. Fu, J. He, P. Ying, X. Zhao, *Adv. Energy Mater.* **2015**, *5*, 1500411.
- [21] Y. Pan, J.-F. Li, *NPG Asia Mater.* **2016**, *8*, e275.
- [22] M. Hong, T. C. Chasapis, Z.-G. Chen, L. Yang, M. G. Kanatzidis, G. J. Snyder, J. Zou, *ACS Nano* **2016**, *10*, 4719–4727.
- [23] T. H. Bauer, *Int. J. Heat Mass Transfer* **1993**, *36*, 4181–4191.

- [24] T. Feng, X. Ruan, *J. Nanomater.* **2014**, 2014, 25.
- [25] V. Chis, I. Y. Sklyadneva, K. A. Kokh, V. A. Volodin, O. E. Tereshchenko, E. V. Chulkov, *Phys. Rev. B* **2012**, 86, 174304.
- [26] W. Liu, K. C. Lukas, K. McEnaney, S. Lee, Q. Zhang, C. P. Opeil, G. Chen, Z. Ren, *Energy Environ. Sci.* **2013**, 6, 552–560.
- [27] W. Liu, X. Tan, K. Yin, H. Liu, X. Tang, J. Shi, Q. Zhang, C. Uher, *Phys. Rev. Lett.* **2012**, 108, 166601.
- [28] T. Yamada, H. Yamane, H. Nagai, *Adv. Mater.* **2015**, 27, 4708–4713.

Manuscript received: December 10, 2016

Final Article published: ■ ■ ■ ■, ■ ■ ■ ■

---

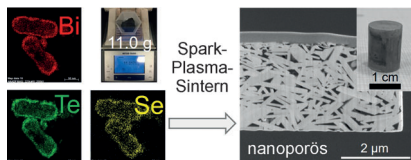
## Zuschriften

VIP

## Nanoporöse Materialien



B. Xu, T. L. Feng, M. T. Agne, L. Zhou,  
X. L. Ruan, G. J. Snyder,  
Y. Wu\*



**Poröse thermoelektrische Komposite** mit einer extrem niedrigen thermischen Leitfähigkeit und hoher Leistungszahl wurden in großen Mengen aus in Lösung synthetisierten hohlen  $\text{Bi}_2\text{Te}_{2.5}\text{Se}_{0.5}$ -Nanostrukturen hergestellt. Die leichtgewichtigen Materialien erfordern weniger Rohmaterial und verbessern die Tragbarkeit thermoelektrischer Komponenten.

Highly Porous Thermoelectric  
Nanocomposites with Low Thermal  
Conductivity and High Figure of Merit  
from Large-Scale Solution-Synthesized  
 $\text{Bi}_2\text{Te}_{2.5}\text{Se}_{0.5}$  Hollow Nanostructures